Angle-and polarization-dependent collective excitation of plasmonic nanoarrays for surface enhanced infrared spectroscopy

Vladimir Liberman,[1]* Ronen Adato,[2,4] Alket Mertiri,[3,4] Ahmet A. Yanik,[2,4] Kai Chen,[2,4] Thomas H. Jeys,[1] Shyamsunder Erramilli,[3,4,5] and Hatice Altug[2,3,4]

[1]*Lincoln Laboratory, Massachusetts Institute of Technology, Lexington, Massachusetts 02420, USA*
[2]*Department of Electrical and Computer Engineering, Boston University, Boston, Massachusetts 02215, USA*
[3]*Division of Materials Science and Engineering, Boston University Boston, Massachusetts 02215, USA*
[4]*Boston University Photonics Center, Boston, Massachusetts 02215, USA*
[5]*Department of Physics & Biomedical Engineering, Boston University Boston, Massachusetts 02215, USA*
**vlad@ll.mit.edu*

Abstract: Our recent work has showed that diffractively coupled nanoplasmonic arrays for Fourier transform infrared (FTIR) microspectroscopy can enhance the Amide I protein vibrational stretch by up to 10^5 times as compared to plain substrates. In this work we consider computationally the impact of a microscope objective illumination cone on array performance. We derive an approach for computing angular- and spatially-averaged reflectance for various numerical aperture (NA) objectives. We then use this approach to show that arrays that are perfectly optimized for normal incidence undergo significant response degradation even at modest NAs, whereas arrays that are slightly detuned from the perfect grating condition at normal incidence irradiation exhibit only a slight drop in performance when analyzed with a microscope objective. Our simulation results are in good agreement with microscope measurements of experimentally optimized periodic nanoplasmonic arrays.

OCIS codes: (240.6680) Surface plasmons; (260.3910) Metal optics; (250.5403) Plasmonics.

References and links

1. R. Adato, A. A. Yanik, J. J. Amsden, D. L. Kaplan, F. G. Omenetto, M. K. Hong, S. Erramilli, and H. Altug, "Ultra-sensitive vibrational spectroscopy of protein monolayers with plasmonic nanoantenna arrays," Proc. Natl. Acad. Sci. U.S.A. **106**(46), 19227–19232 (2009).
2. B. Lamprecht, G. Schider, R. T. Lechner, H. Ditlbacher, J. R. Krenn, A. Leitner, and F. R. Aussenegg, "Metal nanoparticle gratings: influence of dipolar particle interaction on the plasmon resonance," Phys. Rev. Lett. **84**(20), 4721–4724 (2000).
3. T. K. Gaylord and G. R. Kilby, "Optical single-angle plane-wave transmittances/reflectances from Schwarzschild objective variable-angle measurements," Rev. Sci. Instrum. **75**(2), 317–323 (2004).
4. C. P. Burrows and W. L. Barnes, "Large spectral extinction due to overlap of dipolar and quadrupolar plasmonic modes of metallic nanoparticles in arrays," Opt. Express **18**(3), 3187–3198 (2010).
5. A. O. Pinchuk, "Angle dependent collective surface plasmon resonance in an array of silver nanoparticles," J. Phys. Chem. A **113**(16), 4430–4436 (2009).
6. Y. A. Urzhumov and G. Shvets, "Applications of nanoparticle arrays to coherent anti-Stokes Raman spectroscopy of chiral molecules," Proc. SPIE **5927**, 59271D, 59271D-12 (2005).
7. H. P. Paudel, K. Bayat, M. F. Baroughi, S. May, and D. W. Galipeau, "FDTD simulation of metallic gratings for enhancement of electromagnetic field by surface plasmon resonance," Proc. SPIE **7597**, 759706, 759706-8 (2010).
8. F. Le and P. Nordlander, "Optical properties of metallic nanoparticle arrays for oblique excitation using the multiple unit cell method," J. Comput. Theor. Nanosci. **6**(9), 2031–2039 (2009).
9. S. Malynych and G. Chumanov, "Light-induced coherent interactions between silver nanoparticles in two-dimensional arrays," J. Am. Chem. Soc. **125**(10), 2896–2898 (2003).
10. N. Félidj, G. Laurent, J. Aubard, G. Lévi, A. Hohenau, J. R. Krenn, and F. R. Aussenegg, "Grating-induced plasmon mode in gold nanoparticle arrays," J. Chem. Phys. **123**(22), 221103 (2005).
11. N. Félidj, J. Aubard, G. Levi, J. R. Krenn, G. Schider, A. Leitner, and F. R. Aussenegg, "Enhanced substrate-induced coupling in two-dimensional gold nanoparticle arrays," Phys. Rev. B **66**(24), 245407 (2002).

#145572 - $15.00 USD Received 7 Apr 2011; revised 12 May 2011; accepted 12 May 2011; published 24 May 2011

12. Y. Chu, E. Schonbrun, T. Yang, and K. B. Crozier, "Experimental observation of narrow surface plasmon resonances in gold nanoparticle arrays," Appl. Phys. Lett. **93**(18), 181108 (2008).
13. G. R. Kilby and T. K. Gaylord, "Fourier transform infrared transmission microspectroscopy of photonic crystal structures," Appl. Opt. **48**(19), 3716–3721 (2009).
14. B. J. Davis, P. S. Carney, and R. Bhargava, "Theory of midinfrared absorption microspectroscopy: I. Homogeneous samples," Anal. Chem. **82**(9), 3474–3486 (2010).
15. B. J. Davis, P. S. Carney, and R. Bhargava, "Theory of mid-infrared absorption microspectroscopy: II. Heterogeneous samples," Anal. Chem. **82**(9), 3487–3499 (2010).
16. M. J. Nasse, M. J. Walsh, E. C. Mattson, R. Reininger, A. Kajdacsy-Balla, V. Macias, R. Bhargava, and C. J. Hirschmugl, "High-resolution Fourier-transform infrared chemical imaging with multiple synchrotron beams," Nat. Methods **8**(5), 413–416 (2011).
17. R. Bhargava, "Towards a practical Fourier transform infrared chemical imaging protocol for cancer histopathology," Anal. Bioanal. Chem. **389**(4), 1155–1169 (2007).
18. R. Adato, A. A. Yanik, C.-H. Wu, G. Shvets, and H. Altug, "Radiative engineering of plasmon lifetimes in embedded nanoantenna arrays," Opt. Express **18**(5), 4526–4537 (2010).
19. L. Zhao, K. L. Kelly, and G. C. Schatz, "The extinction spectra of silver nanoparticle arrays: influence of array structure on plasmon resonance wavelength and width," J. Phys. Chem. B **107**(30), 7343–7350 (2003).
20. FDTD Solutions, Lumerical, Inc..
21. P. Harms, R. Mittra, and W. Ko, "Implementation of the periodic boundary condition in the finite-difference time-domain algorithm for FSS structures," IEEE Trans. Antenn. Propag. **42**(9), 1317–1324 (1994).
22. A. Taflove and S. C. Hagness, *Computational Electrodynamics. The Finite-Difference Time-Domain Method* (Artech House, 2005), Ch. 13.
23. M. Mishrikey, A. Fallahi, C. Hafner, and R. Vahldieck, "Improved performance of thin film broadband antireflective coatings," Proc. SPIE **6717**, 67102 (2007).
24. N. T. Bliss, R. Bond, J. Kepner, H. Kim, and A. Reuther, "Interactive grid computing at Lincoln Laboratory," Lincoln Lab. J. **16**, 165–216 (2006).
25. E. D. Palik, *Handbook of Optical Constants of Solids* (Academic Press, 1998).
26. G. R. Kilby and Ph. D. Dissertation, *Infrared Methods Applied to Photonic Crystal Device Development* (Georgia Institute of Technology, 2005).
27. T. Tague, (personal communication, 2010).
28. M. Boulet-Audet, T. Buffeteau, S. Boudreault, N. Daugey, and M. Pézolet, "Quantitative determination of band distortions in diamond attenuated total reflectance infrared spectra," J. Phys. Chem. B **114**(24), 8255–8261 (2010).
29. R. F. Curl, F. Capasso, C. Gmachl, A. A. Kosterev, B. McManus, R. Lewicki, M. Pusharsky, G. Wysocki, and F. K. Tittel, "Quantum cascade lasers in chemical physics," Chem. Phys. Lett. **487**(1-3), 1–18 (2010).

1. Introduction

Our recent work has introduced a new ultra-sensitive vibrational spectroscopy tool for protein analysis based on collective excitation of plasmonic nanoantenna arrays [1]. That work demonstrated near-field intensity enhancements in the mid-infrared (IR) of greater than 1000 over incident light intensity near the surfaces of Au plasmonic antenna arrays on Si substrates. In particular, we showed that by appropriate plasmonic array design, this plasmonic enhancement can be accurately tuned to the amide vibrational modes of proteins and can enhance the Reflectance-Absorbance Spectroscopy (RAS) signatures of up to 10^5 as compared to plain substrate response. Tuning the resonance of the nanoplasmonic array to an appropriate vibrational mode requires optimization of several geometric parameters of the array, including the period, the length and the width of the nanostructures. The goal of such array tuning is to couple the plasmonic resonance of the isolated nanostructures to the diffractive mode of the array so as to achieve additional near field reinforcement [2].

While normal angle-of-incidence electromagnetic simulations are typically employed to optimize the plasmonic nanoantenna behavior, such analysis does not appropriately capture array response that would be expected when measured with a microscope objective with a finite numerical aperture. Since mid-infrared objectives commonly use Schwarzschild all-reflective design, only non-normal incidence rays illuminate the sample, whereas the normal incidence rays are blocked by a secondary mirror (Fig. 1). A typical 0.4 NA objective with a 15x magnification may have an illumination cone between 10 to 24 degrees [3]. In this work, we show that a plasmonic array that is optimized for normal incidence illumination will undergo significant de-tuning when examined with a Schwarzschild design objective. Such de-tuning can be especially severe for those arrays that are optimized for the diffractive coupling conditions.

#145572 - $15.00 USD Received 7 Apr 2011; revised 12 May 2011; accepted 12 May 2011; published 24 May 2011

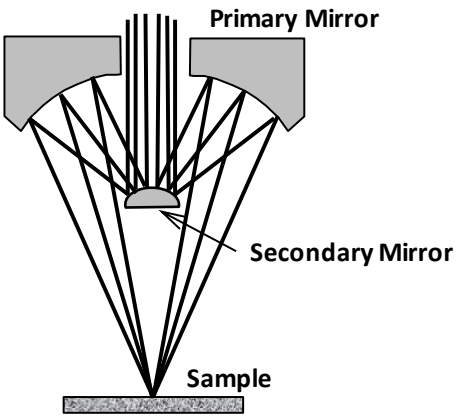

Fig. 1. Optical path of a reflecting Schwarzschild microscope objective.

To our knowledge, this is the first treatment of the effect of the angular spread of the mid-infrared objective on the nanoplasmonic array response. Several earlier papers considered oblique angle of incidence irradiation of coherent plasmonic arrays, both theoretically [4–8] and experimentally [9–12]. However, all those studies were performed in the visible and near-infrared part of the spectrum and the analysis considered plane waves at a single angle of incidence, with no attempt to obtain an averaged response over a full angular cone. Notably, Kilby and Gaylord have analyzed angular-dependent response of photonic crystal structures when probed with an FTIR microscope, and we follow their approach for calculating the intensity-angular-weighting coefficients of the objective response [3,13]. Detailed analysis of sample response when illuminated with a realistic IR objective is of particular interest in absorption microspectroscopy and chemical imaging applications, where signals from homogeneous [14] and non-homogeneous [15] samples can be affected considerably by the numerical aperture. Given that the enhancement of absorption signatures represents a major potential application of plasmonic substrates in the infrared, the analysis of their response under angled illumination presented here is of critical importance to future surface enhanced infrared absorption-reflectance (SEIRA) applications. These applications include both configurations where the signal is obtained from the plasmonic array as a whole and where the spatial resolution afforded by the microscopy approach can provide detailed chemical maps of the sample under investigation [16], e.g. for cancer histopathology [17].

2. Computational approach and geometry

We first compute an electromagnetic response of plasmonic arrays, both in the far-field and the near-field, for a series of plane waves at varying angle of incidence and at two polarizations. For all calculations, grating analysis is performed to determine radiation propagation into the far field. These oblique angle-of-incidence calculations are described in section 3. We then consider typical Schwarzschild objective designs and perform angular and spatial averaging over the surface of the primary mirror to determine the resultant response of different NA objectives. These calculations are described in section 4.

For the analysis, we have chosen two different two-dimensional array geometries (Fig. 2), both of which are tuned for the normal-incidence peak response of the Amide I protein absorption band at 1650 cm^{-1} (Fig. 3). Both geometries consist of periodic Au array nanorods on a Si substrate, similar to the ones fabricated and characterized in our earlier study [1]. For Array I, we computationally optimized the nanorod length of 0.87 μm and a period of 1.75 μm in both directions. For an array with this periodicity, the (1,0) grating order transitions from evanescent to radiative at ~1656 cm^{-1} in the Si substrate. The proximity of the grating transition wavelength to the resonance (peak at ~1650 cm^{-1}) implies an optimal reduction in radiation damping as a result of the diffractive coupling. This is evident in the narrow linewidth of the response (red curve in Fig. 3). For Array II, on the other hand, the periodicity

#145572 - $15.00 USD Received 7 Apr 2011; revised 12 May 2011; accepted 12 May 2011; published 24 May 2011

is reduced so as to diminish the above mentioned diffractive coupling effects. With the reduction in periodicity, the diffractive coupling in the array shifts the resonance peak to shorter wavelengths [1]. Thus, the nanorod length is increased to 0.950 μm in order to compensate for this shift and to obtain a resonance near 1650 cm^{-1}. Radiation damping is therefore more significant in this arrangement leading to the broader peak observed in Fig. 3 (green curve). For both arrays, the nanorods have a width of 230 nm and a height of 70 nm. The incident light polarization is along the long axis of the bar for both arrays. Figure 2(A) summarizes the relevant dimensions of the two arrays whereas Figs. 2(B) and 2(C) represent oblique angle-of-incidence illumination geometry, corresponding to s-polarization (Fig. 2(B)) and p-polarization (Fig. 2(C)). The wireframe boxes at the corners of the nanorods represent electric field (E-field) monitor cubes for assessing hot spots of the structures. In particular, monitors S_2 and S_1 represent the leading and receding edges for s-polarization, whereas monitors P_1 and P_3 represent leading and receding edges for p-polarization, respectively.

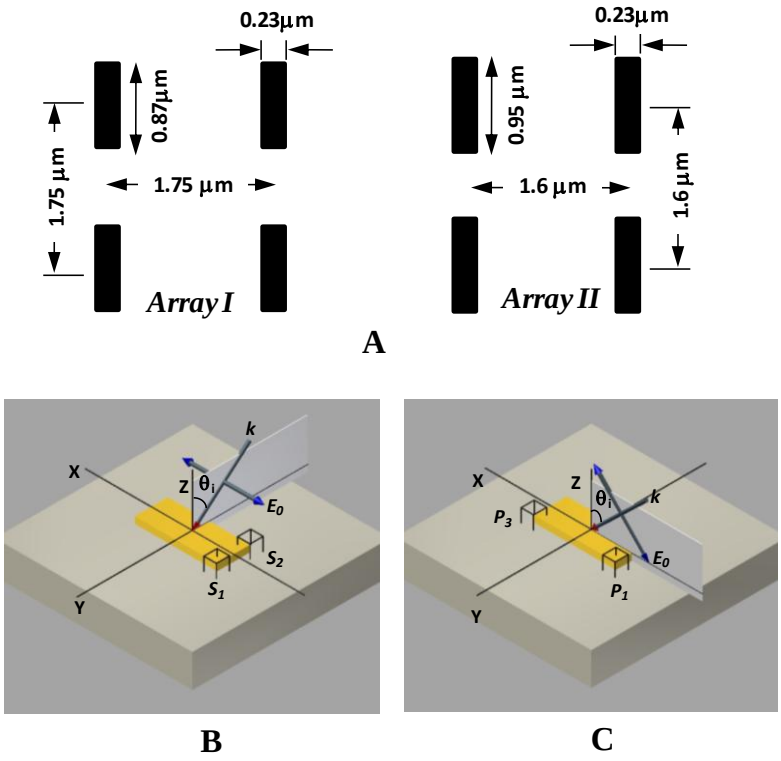

Fig. 2. A. Dimensions of the two arrays simulated in the paper. B&C: Modeled illumination geometry and field monitors for s-polarization (B) and p-polarization (C).

We can assess the strength of the resonance by defining a quality factor (Q-factor) for array reflectance (Fig. 3) as $f/\Delta f_{eff}$. In this expression, f is the wavenumber of the reflectance peak and Δf_{eff} is the width of the peak in terms of maximum reflectance, R_{max}, and bare substrate reflectance, R_{Si}, as the point where array reflectivity is $(R_{max} + R_{Si})/2$. Then the Q-factor of Array I is 12 and that of Array II is 6. The Q-factor of Array II is comparable to the microscope-measured array that has been optimized for collective excitations (see [1], Fig. 3). The peak reflectivity for both arrays (0.83 - 0.85) is substantially higher than that of a randomly-spaced array with a similar pattern density, which is ~0.55 [1]. From separate numerical calculations, the peak electric field intensity at the surface of Array I is nearly twice that of Array II (see also Fig. 7), suggesting that Array I at a normal angle of incidence would offer more absorbance sensitivity.

#145572 - $15.00 USD Received 7 Apr 2011; revised 12 May 2011; accepted 12 May 2011; published 24 May 2011

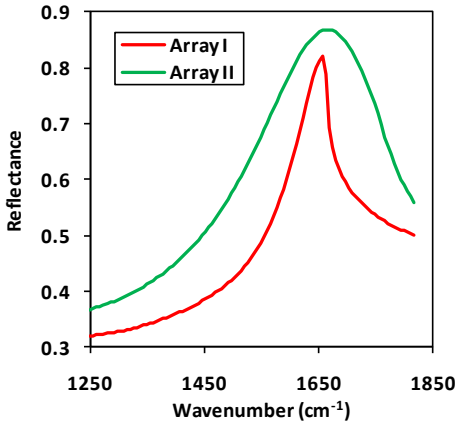

Fig. 3. Computed normal incidence reflectance of the two array geometries of Fig. 2(A).

3. Oblique Angle-of-Incidence (AOI) plane wave response

The Finite Difference Time Domain Method (FDTD) is used for this work because of its flexibility in modeling nanostructures with arbitrarily complex geometries. In our previous work on nanoplasmonic arrays [1], results of normal incidence FDTD calculations correlated well with experimental measurement. Alternatively, semi-analytical theories such as Coupled Dipole Approximation have been used to model scattering from plasmonic arrays, but are appropriate only for modeling particles in a homogeneous background (no substrate) and cannot be used to obtain near-field distributions for most particle geometries [18,19].

Extension of FDTD method to oblique AOI calculations causes two complications: (1) Periodic Boundary Conditions (PBCs) that are typically used for normal incidence array simulations in FDTD can no longer be used for oblique incidence because of the phase mismatch across the boundaries, and (2) broad spectral simulations that are inherent in FDTD method result in each frequency component propagating at a different angle. These complications have been addressed by the FDTD software from Lumerical Solutions [20]. First, for the oblique AOI, Bloch boundary conditions are used, also known as the "Sine and Cosine" method [20,21]. This method splits the simulation into two separate grids and excites the grids with sin (ωt) and cos (ωt) time dependencies, respectively. The method has an advantage in that the stability condition for simulation is the same as for the normal-incidence FDTD algorithm, unlike split-field methods which require smaller meshing and finer time steps [22]. The disadvantage of this method is that it loses the broadband capability of FDTD modeling as each frequency has to be solved separately. Secondly, since each oblique angle-of-incidence simulation run contains a spread of angles *vs.* frequency, we perform an angular parameter sweep followed by a series of 1D interpolations of the data onto a common source angle vector. A similar interpolative procedure has been independently demonstrated by Mishrikey *et al.* [23]. The implementation of the above modifications to the standard FDTD method carries a significant computational overhead, for both memory requirements and computation runtime. We, thus, performed simulations on a high performance computing cluster at MIT Lincoln Laboratory, LLGrid [24], where a single job was launched on up to 128 processors.

In order to keep the computational times manageable, we limited the length of the simulation runs for oblique incidence simulations to achieve acceptable convergence of the electric fields, as specified by an auto shutoff level of 10^{-3} for the E-field decay in the simulation region. Slight ripple, observed in Figs. 4 and 6 is the result of this compromise. However, this ripple does not affect the conclusions of our paper.

For the optical constants of Au, we use data in the mid-IR range from Palik [25]. The sampled data are fit to the Kramers-Kronig consistent multi-coefficient model [20]. While the

#145572 - $15.00 USD Received 7 Apr 2011; revised 12 May 2011; accepted 12 May 2011; published 24 May 2011

fabricated Au nanostructures include a thin Ti adhesion layer (≤5 nm thickness), we verified in independent simulations that its presence does not affect the results presented here within 5% accuracy. Simulations were performed using plane wave incident source with a wavelength range from 5.5 to 8 μm (from 1820 to 1250 cm^{-1}). The substrate plane is the XY coordinate plane in our simulation with the long axis of the nanorod along the X direction (Fig. 2).

For the angle-of-incidence sweeps, the projection of the incident electric field vector onto the array surface was always aligned along the long axis of the nanorods (Figs. 2(B) and 2(C)). From our previous work, excitation along the long axis causes much stronger coupling of the field to the nanorods than that along the short axis [1]. The angular sweeps are performed from near-normal incidence (5 degrees) to 30 degree incidence for both s- and p-polarization of light with respect to the silicon substrate (Fig. 2(B) and 2(C)).

For all the simulations, we computed far-field reflectance data of the nanorod arrays. The data were obtained by first computing a backscatter response over a half-plane located several microns above the Si substrate. Since we simulate infinitely periodic arrays, the far-field projection of the data reduces to grating order analysis. While higher diffractive orders can propagate in the high-index silicon substrate, only the (0,0) order propagates in air towards the detector for all the array geometries and angles of incidence considered. The reflectance response as a function of angle was calculated in one-degree increments using the angular parameter sweep described above.

In Figs. 4(A) and 4(B) we show a series of reflectance curves for various incident angles for s- and p-polarizations for Array I nanostructure. Rapid changes in reflectance for Array I as a function of angle of incidence occur at either polarization even for angles of incidence as low as 5 degrees. For s-polarization (Fig. 4(A)), a broad shoulder develops at higher incidence angles around 1450 cm^{-1}, while the peak reflectance decreases and then begins to level off (see also Fig. 5). For p-polarization (Figs. 4(B) and 5), the peak reflectance decreases with angle of incidence without saturation. For both polarizations, only a slight blue shift (≤ 10 cm^{-1}) of the main peak is observed with increasing angle of incidence.

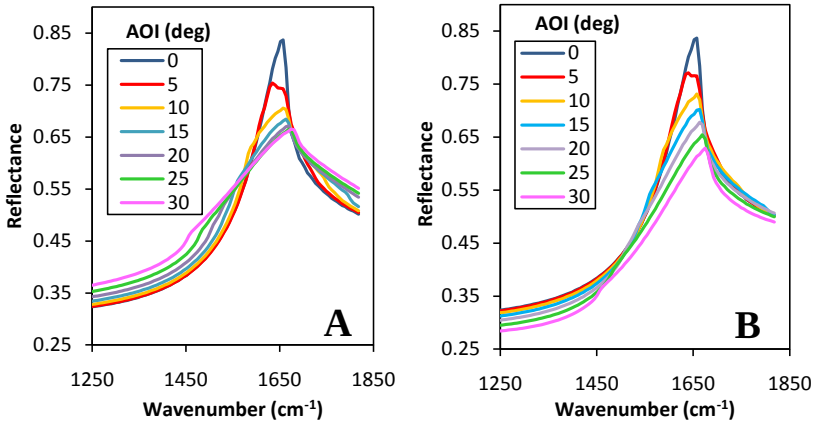

Fig. 4. Spectral reflectance for Array I for A. s-polarization and B. p-polarization for several angles of incidence.

By contrast to Array I, much less change in performance is observed in reflectance spectra of Array II with angle of incidence. As shown in Fig. 5, the peak reflectance for Array II remains fairly flat till 20 degree angle and then decreases slightly in an oscillatory fashion. Even at the highest incidence angle considered here (30 degrees), the peak reflectance reduction for Array II is three times smaller than for Array I.

#145572 - $15.00 USD Received 7 Apr 2011; revised 12 May 2011; accepted 12 May 2011; published 24 May 2011

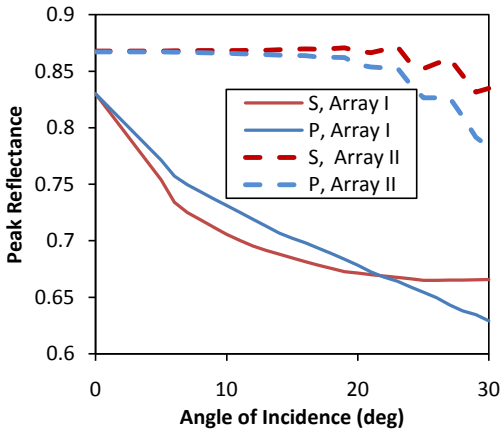

Fig. 5. Dependence of peak reflectance on an angle of incidence for arrays I and II at two incident polarizations.

In order to gain more insight into the near-field radiation coupling mechanisms, we have computed spectral dependences of the near field intensity for our nanostructures. From previous work [1], maximum field intensity occurs in the lower corners of the nanorod structures, adjacent to the high index silicon substrate. For both Arrays I and II, we analyzed corner hot spots labeled S_1 and S_2 for s-polarization (Fig. 2(B)) and P_1 and P_3 for p-polarization (Fig. 2(C)). Because of the array symmetry, the above corners are sufficient for describing all the hot spots. Figure 6 shows spectral dependence of the near-field hot spot for Array I for several angles of incidence at s- and p-polarizations. Major trends are a significant reduction in intensity and a decrease of Q-factor with increasing angle. No new spectral features are observed.

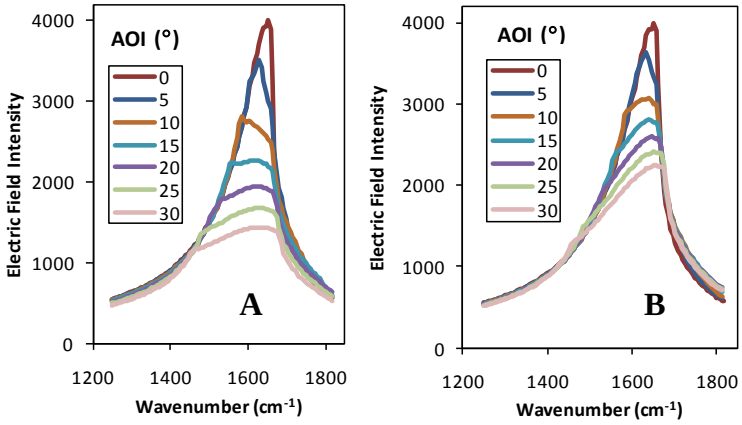

Fig. 6. Spectral dependence of peak near field intensity vs. angle of incidence for Array I: A. Corner S_1 and B. Corner P_1.

Figure 7 summarizes angular-dependent near-field trends for all the hot spots analyzed for both array geometries. All the hot spots for array I substantially decrease in intensity with angle of incidence, indicating a reduced coupling to the nanoplasmonic array. By contrast, much less intensity decrease is observed for array II. Furthermore, for all but one hot spot (P_3), there is a cross-over point between 15 and 20 degrees beyond which array II outperforms array I with respect to field intensity. Finally, for array I, there is a stronger field coupling for the receding edge of the nanorod, P_3, vs. the leading edge, P_1.

#145572 - $15.00 USD Received 7 Apr 2011; revised 12 May 2011; accepted 12 May 2011; published 24 May 2011

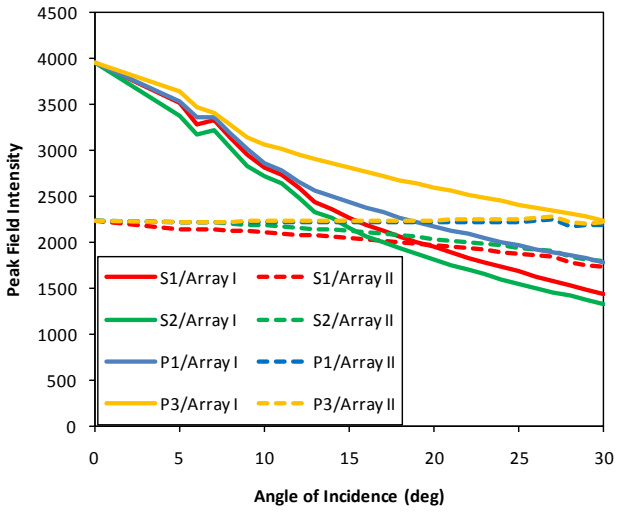

Fig. 7. Peak field intensity vs. angle of incidence for all field monitors of Figs. 2(B) and 2(C) for both array geometries.

A previous study suggested that an increase in the angle-of-incidence θ for a nanoplasmonic grating can be compared to a normal incidence irradiation with a corresponding increase of the array periodicity by $1/\cos(\theta_i)$ [11]. The increase in periodicity would similarly result in array detuning as the critical grating period is no longer maintained. To explore this analogy, we modeled the reflectance and the near field response of Array I at normal incidence, while changing its periodicity in the Y dimension, and compared these results to the s-polarization angular sweep. Thus, at normal incidence, the period was varied from 1.75 μm to 1.75/cos(30°) = 2 μm. Comparison of Fig. 8(A) with Fig. 4(A) and of Fig. 8(B) with Fig. 6(A) does show a similar peak reduction between an angular sweep and a period sweep at normal incidence. However, the period sweep data overestimate the reflectance reduction and underestimates the field intensity reduction as compared to the angular sweep. Additionally, the period sweep data show a pronounced red shift of the resonance which is not observed in the angular sweep. Thus, the seemingly intuitive geometric analogy between a periodicity increase and an angle-of-incidence increase does not fully apply in this case.

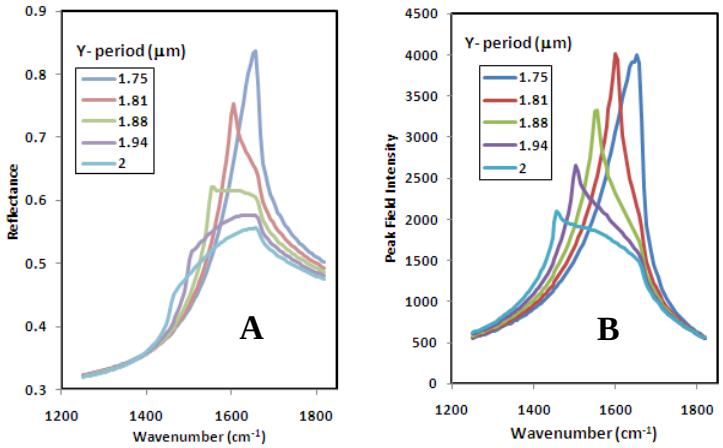

Fig. 8. Array I response for normal incidence irradiation for A. Reflectance and B. Peak field intensity as the period along the Y direction is changed.

#145572 - $15.00 USD Received 7 Apr 2011; revised 12 May 2011; accepted 12 May 2011; published 24 May 2011

For a more complete understanding of the angle-of-incidence data presented in Fig. 4 we need to consider momentum conservation of the grating coupling phenomenon, expressed as

$$k_{sub} = k_{inc} \pm G_x \pm G_y \tag{1}$$

In the above, k_{inc} and k_{sub} refer to the tangential momentum components of the incident and the substrate-propagating waves, respectively, and G_x and G_y are the momentum vectors provided by the square lattice. Equation (1) yields the following relation for the different grating transition wavelengths $\lambda_{i,j}$

$$\left(\frac{2\pi}{\lambda_{i,j}} n_{sub}\right)^2 = \left(\frac{2\pi}{\lambda_{i,j}} \sin\theta_i \cos\phi + i\frac{2\pi}{d}\right)^2 + \left(\frac{2\pi}{\lambda_{i,j}} \sin\theta_i \sin\phi + j\frac{2\pi}{d}\right)^2 \tag{2}$$

In the above, n_{sub} is the substrate index (assuming n = 1 for the incident medium), θ_i is the angle of incidence, and ϕ is the azimuthal angle so that $\phi = \pi/2$ and 0 correspond to s-and p-polarizations, respectively (Figs. 2(B) and 2(C)). Additionally, i = 0, ± 1,… and j = 0, ± 1,… represent different orders of the grating vectors.

Solutions of Eq. (2) for $\lambda_{i,j}$ vs. θ_i for the three orders, *(i,j)* = (0,1) (1,0) and (–1,0) are shown in Fig. 9. The coupling of the localized surface plasmon mode of the nanorod to these diffraction orders is responsible for the variations in spectral shapes in the Fig. 4. A dipole antenna radiates preferentially perpendicular to its axis of polarization; therefore, the antenna should couple more efficiently into the $j = 0$ modes for s-polarization than for p-polarization. Shoulder positions of Fig. 4(A) show excellent agreement with the spectral position of the $j = 0$ diffraction orders for the corresponding angles of incidence from Fig. 9. On the other hand, p-polarization is not expected to couple to the $j = 0$ mode; thus, no such features are observed in Fig. 4(B). Additionally, the overall decrease in reflectance in Fig. 4(B) arises from the fact that the projection of the electric field along the nanorods axis is decreased with increasing angle of incidence for p-polarization.

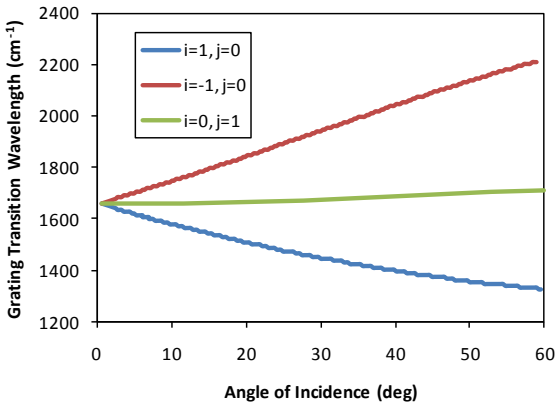

Fig. 9. Grating transition wavelengths for the first three orders vs. the angle of incidence.

4. Schwarzschild objective response to nanoplasmonic arrays

Having characterized the plane-wave response of the two plasmonic array geometries, we now compute the expected angular-averaged response for a Schwarzschild objective with central obscuration. We adopt the approach of Gaylord and Kilby [3] who consider measured reflectance of an objective as an incoherent weighted sum of the plane-wave reflectances at various angles of incidence. Additionally, we perform area-weighted signal average over the surface of the primary objective mirror, which we assume to be spherical. In spherical coordinates, θ is the polar angle, ϕ is the azimuthal angle, $r(\theta, \phi)$ are plane wave reflectances

#145572 - $15.00 USD Received 7 Apr 2011; revised 12 May 2011; accepted 12 May 2011; published 24 May 2011

as a function of angle and $A(\theta, \phi)$ are weighting coefficients for the microscope reflectance as a function of angle. We assume that the major source of differences in $A(\theta,\phi)$ is a hot filament source emission non-uniformity and alignment as opposed to differences in mirror reflectivity or its response to incident polarization. Furthermore, assuming azimuthal symmetry for the microscope weighting coefficients, the ϕ integration becomes trivial. We obtain for the total objective transmission $R(\lambda)$:

$$R(\lambda)=\frac{\int_{\theta\min}^{\theta\max} 0.5\left[r_s(\theta)+r_s(\theta)\right]A(\theta)\sin\theta d\theta}{\int_{\theta\min}^{\theta\max} A(\theta)\sin\theta d\theta}=\frac{\sum_{\theta\min}^{\theta\max} 0.5\left[r_{s,i}+r_{p,i}\right]A_i\sin\theta}{\sum_{\theta\min}^{\theta\max} A_i\sin\theta} \quad (3)$$

In Eq. (3), the last step simply involves replacing the integral by a discrete sum over angles as computed in section 3. The angular acceptance range depends on a particular objective design and NA. For typical commercial reflecting objectives, the angular range is 10 to 24 degrees for 0.4 NA and 10 to 30 degrees for 0.5 NA [3]. The reflectance weighting coefficients will sensitively depend on the source alignment and, in fact, can be tailored to obtain asymmetric source emission in a relatively narrow cone [26]. However, for a proper factory aligned source, we may assume that the source radiance is relatively uniform over the allowed angle space, that is A_i ~1 for all θ within the angular acceptance range [27].

We compute objective response for 0.4 and 0.5 NA objectives for Arrays I and II (Fig. 10). For either Array I or Array II, increase of NA from 0.4 to 0.5 causes little additional change in response. However, the initial impact on Array I is a lot more severe: a 20% relative drop in reflectance as compared to a 2 - 4% reflectance change for Array II. The reflectance peak shift is 10 cm^{-1} for Array I and −25 cm^{-1} for Array II. By comparison, the full width at half maximum (FWHM) of silk fibroin Amide I absorption band is 50 cm^{-1} [28]. The Q factor of Array I drops from 12 at normal incidence to ~5 for a 0.4 NA objective, whereas the Q-factor of Array II drops from 6 at normal incidence to ~5.4 for 0.4 NA.

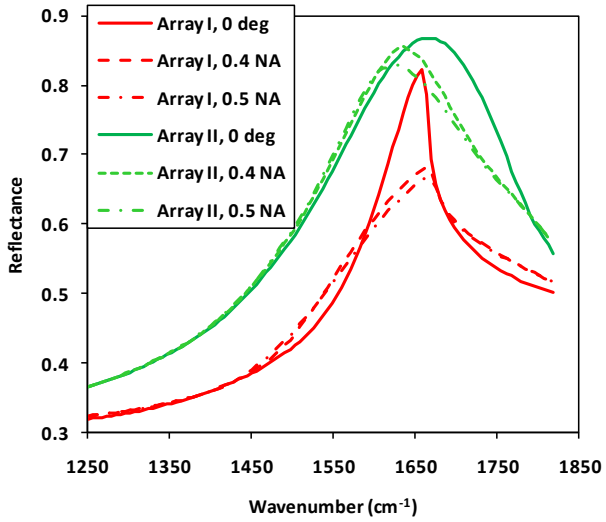

Fig. 10. Response of Arrays I and II when illuminated and measured with a Schwarzschild microscope objective for two different NAs, as compared to normal-incidence response.

While the performance of the Array I is clearly degraded more severely than that of Array II, the ultimate array performance is derived from its sensitivity to absorbance changes of thin protein layers. Fundamentally, this absorbance enhancement depends on the interaction of the electric field at the surface of the nanorod with the dipole moment of the adsorbed protein monolayer, appropriately averaged over space and over a range of incident angles. Computationally, the measured absorbance enhancement can be obtained by comparing

#145572 - $15.00 USD Received 7 Apr 2011; revised 12 May 2011; accepted 12 May 2011; published 24 May 2011

reflectance from a bare nanoplasmonic array to that covered by a protein adlayer, where both reflectances are appropriately angle-averaged, according to Eq. (3).

We note that our experimentally tuned grating-coupled arrays previously measured with an FTIR microscope [1] display similar linewidth and peak reflectance to that of Array II in this study. Thus, such geometry may represent the best compromise for the diffraction-coupled enhancement that can be obtained with an extended angular cone illumination. On the other hand, better resonance matching and, perhaps, better detection sensitivity may be achieved with laser illumination mid IR sources, such as quantum cascade lasers (QCLs) [29].

5. Conclusions

Using oblique angle-of-incidence simulations, we have analyzed the response of plasmonic diffractively coupled nanoarrays under irradiation conditions of a typical Schwarzschild objective.

We find that arrays that are perfectly tuned at normal incidence to the diffractively coupled condition undergo substantial change in reflectivity and near field enhancement even for modest departures from the normal irradiation. Array detuning is caused by increased dephasing of coherent oscillations for increased angles of incidence, manifested by drop in resonant peak intensity, both in the far- and the near-fields, but only a modest peak shift. These detuning effects lead to a 20% drop in reflectance resonance for an objective illumination at 0.4 to 0.5 NA as compared to the normal incidence illumination. On the other hand, an array that is slightly detuned from the normal-incidence grating coupling condition undergoes only a modest change in response for a non-normal incidence irradiation with a Schwarzschild objective. The peak reflectance and linewidths of such arrays are consistent with the nanoplasmonic arrays that have been empirically optimized utilizing a commercial FTIR microscope [1]. An explicit calculation of relative absorbance enhancement of these two arrays should consider a response of a protein-covered surface.

The detuning of plasmonic arrays for non-normal incidence suggests that numerical optimization strategies of such structures must consider the exact irradiance profile of illumination and collection optics instead of relying on normal incidence results. The results also suggest that interrogation of these plasmonic arrays with collimated beams such as obtained from a quantum cascade laser source [29] may allow additional sensitivity improvement of the plasmonic arrays beyond what is currently realizable with microscope objectives.

Acknowledgments

The Lincoln Laboratory portion of this work was sponsored by ASD(R&D) under Air Force contract no. FA8721-05-C-0002. Opinions, interpretations, conclusions and recommendations are those of the authors, and do not necessarily represent the view of the United States Government. The Boston University portion of this work was supported in part by an NSF MRI award (SE) and an NSF SGER award (HA), and the Boston University Photonics Center and Army Research Laboratories. One of the authors, AM, gratefully acknowledges support from MIT Lincoln Laboratory.

#145572 - $15.00 USD Received 7 Apr 2011; revised 12 May 2011; accepted 12 May 2011; published 24 May 2011